RSC Applied Interfaces

ROYAL SOCIETY OF CHEMISTRY

PAPER

View Article Online
View Journal | View Issue

Cite this: *RSC Appl. Interfaces*, 2026, **3**, 913

Interfacial control as a strategy for advanced catalyst layer architectures in PEMFCs

Emanuele Magliocca,[a] Shangwei Zhou,[a] Dan J. L. Brett[b] and Thomas S. Miller *[ac]

Interfaces within polymer electrolyte membrane fuel cells (PEMFCs) dictate proton transport, gas diffusion, and water management – processes that ultimately control power output, efficiency, and durability. Conventional catalyst layers neglect these interfacial dynamics, resulting in severe losses under low humidity and high current density. Here, we introduce an interfacial engineering strategy using a dual-nozzle ultrasonic spray technique that independently deposits Pt/C catalyst and Nafion ionomer, enabling precise control of ionomer distribution without complex multi-ink formulations. This design creates a continuous transition: high ionomer content near the membrane to minimize proton resistance and dehydration, and reduced ionomer near the microporous layer (MPL) to enhance oxygen access and water removal, while enabling the *in situ* formation of the triple phase boundary (TPB). Electrochemical testing across humidity regimes, supported by impedance spectroscopy and accelerated degradation protocols, shows that interfacially optimized layers deliver peak power densities of 803 mW cm^{-2}, 20–30% higher than uniform or inverted designs, and retain superior electrochemical surface area (ECSA) after 30 000 cycles. These results establish interfacial control as a critical design principle for next-generation PEMFC catalyst layers, offering a scalable route to improved performance and long-term stability.

Received 7th February 2026,
Accepted 14th April 2026

DOI: 10.1039/d6lf00036c

rsc.li/RSCApplInter

1. Introduction

Electrochemical devices such as electrolysers, redox flow batteries, and fuel cells all rely on membrane electrode assemblies (MEAs) to enable efficient ion and electron transport.[1–3] Among electrochemical systems, polymer electrolyte membrane fuel cells stand out for their ability to deliver high power density with zero emissions, making them central to decarbonizing transport and stationary energy sectors.[1–3] However, large-scale adoption remains constrained by high material costs and persistent performance limitations. These challenges are most acute in the cathode catalyst layer (CL), where the oxygen reduction reaction (ORR) occurs and where interfacial phenomena strongly influence overall cell behaviour.[4,5]

In conventional PEMFC designs, the CL is fabricated with a uniform distribution of Pt catalyst and ionomer to form the triple-phase boundary, enabling electrochemical reactions.[4,5] This approach assumes that uniformity ensures optimal performance, yet it overlooks the complexity of interfaces within the MEA. When these interfaces are poorly managed, local gradients in ionic potential, oxygen concentration, and water content emerge during operation, leading to uneven catalyst utilization and accelerated degradation of both catalysts and supports.[6–8]

Given these intrinsic interfacial anisotropies, strategies that deliberately tailor interfacial architecture – rather than relying on homogeneous designs – are essential to improve performance and durability.[9]

A growing body of research has demonstrated that tailoring material distribution within the catalyst layer can improve fuel cell performance and reduce material demand.[10] Recent studies have highlighted the importance of advanced material design and functional architectures within membrane electrode assemblies (MEAs) to improve transport processes, catalyst utilization, and overall fuel cell performance.[11,12] Historically, this has been approached through gradient engineering, primarily in two directions: through-plane (TP) along the *Z*-axis, from the membrane/CL interface toward the gas diffusion medium (GDM), and in-plane (IP) along the *X*–*Y* plane, from gas inlet to outlet, to counteract reactant depletion.[10] For example, grading catalyst loading along the flow field has been shown to mitigate local current density variations and improve reactant distribution.[13–18] In-plane strategies therefore aim to address depletion effects, refining CL composition to balance proton transport with mass transport efficiency.

[a] *Electrochemical Innovation Lab, Department of Chemical Engineering, University College London, London WC1E 7JE, UK. E-mail: t.miller@ucl.ac.uk*
[b] *Prosemino Limited, The Paper Yard, Canada Water, London, SE16 7LG, UK*
[c] *Advanced Propulsion Lab, UCL East Marshgate, 7 Sidings Street, Stratford, London, E20 2AE, UK*

The most critical transport processes – proton conduction, water retention, and oxygen access – are not simply bulk phenomena; they are controlled by the interfaces within the MEA. The CL–membrane interface dictates ionic continuity and hydration, while the CL–microporous layer interface governs gas permeability and water removal. Catalyst–ionomer interfaces define the connectivity of the triple-phase boundary and influence charge transfer kinetics. When these interfaces are poorly optimized, performance losses and accelerated degradation follow.[19–21]

Through-plane ionomer gradients have been widely explored because they directly affect these boundaries, yet the literature on catalyst gradients reveals conflicting trends. Many studies report improved performance when catalyst loading is increased toward the membrane,[22–27] while others find advantages with higher loadings near the GDM under certain conditions.[28–32] These discrepancies arise from competing interfacial requirements: enhanced proton conduction and adhesion near the membrane *versus* improved oxygen transport and water management near the GDM. Operating conditions such as relative humidity and current density strongly influence which interface dominates performance.

Overall, while gradient designs can boost performance, their optimal configuration is not universal. This underscores a critical insight: interfaces – not just gradients – must be deliberately engineered to achieve robust, high-performance catalyst layers across diverse operating regimes.

Parallel efforts have focused on optimizing TP ionomer distribution, traditionally implemented as a uniform ionomer-to-carbon (I/C) ratio across the CL thickness.[33,34] Because ionomer films govern proton conduction from the membrane and shape the pore architecture for reactant access, their spatial distribution is critical. Proton transport is most efficient near the membrane interface and decreases toward the GDM as protons are consumed;[35] therefore, increasing ionomer content near the membrane is a logical design strategy.

This concept is consistent with theoretical and modelling studies,[36–39] which predict that optimal catalyst layer architectures involve higher ionomer content near the membrane interface to facilitate proton transport, combined with lower ionomer content toward the GDM/MPL interface to enhance oxygen diffusion and water removal. The gradient configuration explored in this work follows these design principles by introducing a controlled through-plane variation in ionomer distribution.

Wang *et al.*[36] introduced a numerical model using a triple-coated layer (TCL) with an ionomer gradient increasing toward the membrane, predicting modest performance gains over uniform CLs due to improved proton conduction and mass transport. Conversely, gradients with higher ionomer content near the GDM reduced performance because of elevated transport resistance and diminished proton conductivity. Experimental validation by Xie *et al.*[37] compared uniform and graded TCLs, where the graded electrode comprised three sublayers with Nafion contents ranging from 20 to 40 wt%. At intermediate and high current densities, increasing ionomer content near the CL/membrane interface improved cathodic performance, while reversing the gradient caused significant losses. This improvement was attributed to higher ionic conductivity near the membrane and enhanced gas diffusion near the GDM, supported by a complementary interparticle pore gradient.

However, these approaches relied on hand-spraying distinct inks with varying Nafion loadings, producing discrete layers rather than a continuous gradient, as confirmed by cross-sectional EDS – highlighting poor reproducibility and scalability. A similar double-coated layer (DCL) configuration reported by Kim *et al.*[38] showed improved performance for TP ionomer gradients increasing toward the PEM, primarily due to better mass transport, yet required manual spraying of five distinct inks – an impractical and non-scalable method. Chen *et al.*[23] reported peak power density gains of 25.4% at 80% RH and 104.2% at 20% RH using DCLs with higher ionomer content near the membrane, while Shahgaldi *et al.*[39] observed a 13% improvement under similar configurations. Despite these promising results, most studies lacked morphological confirmation and remained constrained by stepwise layering, which introduces interfacial defects and limits manufacturing scalability.

Step-function designs such as DCLs and TCLs dominate current literature, but their abrupt material transitions create interfacial resistances, mechanical instability, and localized defects. Sequential spray-coating of multiple catalyst inks remains the most common fabrication route, yet this approach introduces significant complexity, including interlayer adhesion problems, defect formation, and strong sensitivity to deposition parameters. Attempts to refine these concepts through more elaborate architectures – such as five-layer CLs[40] – deliver only incremental gains in performance and durability while further complicating manufacturing and limiting scalability.

The reliance on discrete layering and sequential spraying poses additional challenges for reproducibility and automation, underscoring the need for advanced methods that can produce continuous, smooth, and scalable interfacial architectures. Such approaches must eliminate abrupt boundaries, maintain structural integrity, and enable precise control of material distribution to optimize proton conduction, gas transport, and water management simultaneously.

In this work, we move beyond compositional gradients to address the fundamental challenge of interfacial control within the catalyst layer. Rather than focusing on multi-component gradient architectures, our approach targets the critical boundaries that govern PEMFC performance: the CL–membrane interface, the CL–microporous layer interface, and the catalyst–ionomer interface. Using a dual-nozzle ultrasonic spray technique, we independently deposit Pt/C catalyst and Nafion ionomer, enabling precise modulation of ionomer coverage without the complexity of multiple ink formulations. This strategy creates a continuous interfacial

transition – high ionomer content near the membrane to minimize proton resistance and dehydration, and reduced ionomer near the MPL to enhance oxygen access and water removal – while preserving structural integrity across the layer.

Electrochemical evaluation under varying humidity and current densities, combined with impedance spectroscopy and accelerated degradation testing (ADT), demonstrates that interfacially optimized layers deliver superior performance and durability compared to uniform or inverted designs. Cross-sectional EDS confirms the absence of abrupt boundaries, validating the smooth interfacial architecture. By reframing catalyst layer design around interfaces rather than bulk gradients, this work establishes a scalable, automation-ready pathway for next-generation PEMFCs. While the present deposition parameters were optimized to maximize compositional control, resulting in longer coating times, the process inherently offers high material utilization efficiency (≈75–80%) and can be further optimized in terms of ink concentration and flow rate to approach industrially relevant deposition rates; moreover, its compatibility with programmable spray paths and automated ink refill system makes it a promising candidate for future scale-up, including potential adaptation to roll-to-roll manufacturing. The principles demonstrated here extend beyond fuel cells to other electrochemical systems, where interfacial phenomena dictate efficiency and lifetime.

2. Methodology

Ink preparation, spray coating, electrode fabrication and testing

Materials. Alcohol-based Nafion dispersion D2021 (1100 EW, 20 wt%); Platinum, nominally 20 wt% on high surface area advanced carbon support powder (HiSpec 3000, Alfa Aesar) and Freudenberg H23C8 (205 μm), were used along with a gas diffusion media, consisting of a carbon-fiber paper, PTFE-treated (5 wt%), with a carbon microporous layer 15 μm thick on one side, were purchased from Fuel Cell Store. 99.9% isopropanol was purchased from Sigma-Aldrich. High-purity water (18.2 MΩ cm) was used in this work. All coating layers were obtained with an automatic ultrasonic spray coater (USC, ExactaCoat) from SonoTek, equipped with two independent AccuMist nozzles (120 kHz). A 1 mm-thick polycarbonate mask was used during coating.

CL fabrication

The cathode CLs were deposited onto the GDM; *via* a layer-by-layer method using a robotic ultrasonic spray set up with two independent nozzles. The composition and preparation of catalyst ink play a critical role in defining the microstructure of the catalyst layer. To develop complex and innovative CL architectures, a carefully tuned interplay of ink formulation, deposition techniques, and advanced manufacturing approaches is essential.[41] In our setup, the Nafion dispersion and the Pt/C suspension are prepared separately in two different glass jars, as they are utilized independently. Moreover, to achieve a more accurate and reproducible gradient design, the use of diluted inks is essential for improved control over the layer-by-layer deposition process. So, 64 mg of Nafion were dispersed in 200 mL of DI water and 100 mg of Pt/C suspended in 200 mL mixture of DI water and isopropanol (1 : 1), resulting in concentrations of 0.32 mg mL^{-1} and 0.5 mg mL^{-1}, respectively. Both dispersions were sealed with airtight caps to prevent solvent evaporation and left under magnetic stirring overnight. As a final step in the ink preparation, they were placed in an ultrasonic bath for 30 min prior to use in the coating process, and utilized within three days. When the prepared ink was not used for coating, it was placed under magnetic stirring. Before reuse, the prepared and stirred ink was introduced into an ultrasonic bath for at least 30 min, same treatment was adopted for the Nafion dispersion. The decision to prepare two separate dispersions – one for Nafion and one for Pt/C – was driven by the need to prevent agglomeration, which typically leads to the formation of larger ionomer domains.[42] This phenomenon is primarily attributed to electrostatic interactions between sulfonic acid groups and platinum particles, which not only cause catalytic poisoning but also create highly tortuous pathways for oxygen transport.[43,44] To overcome these limitations, an *in situ* formation of the TPB was preferred, enabling the development of a more controlled and interconnected catalyst layer microstructure during the deposition. This approach also provided the opportunity to precisely fine-tune the composition of the layer-by-layer microstructure, crucial for creating a graduated CL architecture. This fabrication method was made possible by the dual independent robotic arms of the ultrasonic spray coater, which allowed for the precise and controlled alternating co-spraying of the two components, as represented in the schematics in Fig. 1a.

Automated ultrasonic spray setup. The spray bench is composed of two independent mobile spraying nozzles in 3 dimensions (x, y and z) and a heating plate equipped with a vacuum suction bed to securely hold the coating substrate in place. The two jars containing the spraying suspensions, kept under continuous gentle magnetic stirring, are connected to two 25 mL syringes (Gastight Model 1025), through connecting tubes and automated valves, both attached to two distinct syringe pumps, controlled by the integrated software. Due to the mobility of the nozzle head, the length of the connecting tubes cannot be neglected. Therefore, a dead volume of about 10 mL must be taken into account when preparing the dispersions. The flow rate, the speed and the ultrasonic power of both the spray nozzles were fixed at 0.1 mL min^{-1}, 5 mm s^{-1} and 1.5 W, respectively, *via* the Sono-tek software. The low flow rate was primarily selected to prevent the coffee-ring effect,[45] which can result from substrate flooding due to the ink not evaporating fast enough during the deposition process. Additionally, a 0.1 mL min^{-1} flow rate allowed for precise control over the formation of the layer-by-layer microstructure. The shaping air pressure remained at 1 bar throughout the process. The temperature of the heating plate was set at 80 °C, to ensure an optimal evaporation time

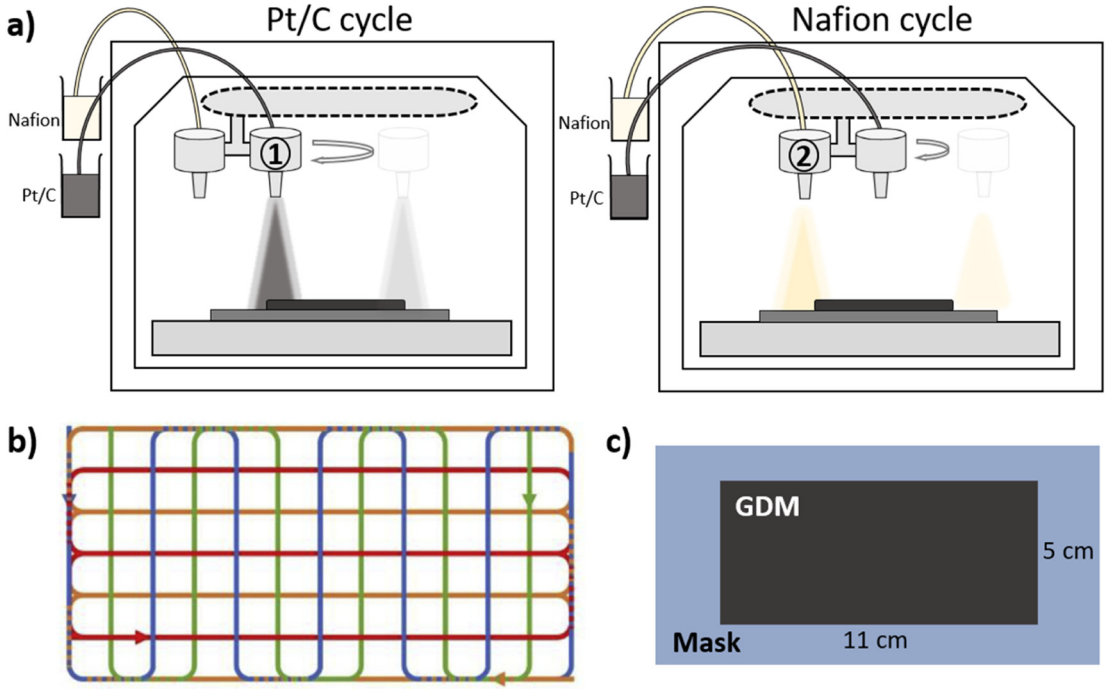

Fig. 1 a) Schematic illustration of the USC system used in this work, with two independent nozzles. Example of the two alternating spraying configurations, nozzle 1 for the Pt/C cycles and nozzle 2 for the Nafion cycles. b) Example of the serpentine spray pattern adopted for each cycle, 1st run path in blue (vertical), 2nd run path in orange (horizontal), 3rd run offset path in green (vertical) and 4th run offset path in red (horizontal). c) Schematic of the coating setup and mask configuration used in this work.

of the suspensions, in line with recent studies employing comparable flow rates;[46] the height of the ultrasonic nozzles was fixed at 10 cm. A serpentine pattern was chosen for the spray coating with a pace of 4 mm between each line. To ensure a homogeneous coating, two vertical and two horizontal serpentine paths, offset by half of the pace relative to one another, were alternated to effectively cover the blank gaps between adjacent serpentine lines[47] (Fig. 1b). Due to the curvature at the turning points of the serpentine pattern, changes in spray direction led to heterogeneity along the edges of the coated area. Therefore, the use of a mask is crucial to achieve well-defined edges, however the thickness

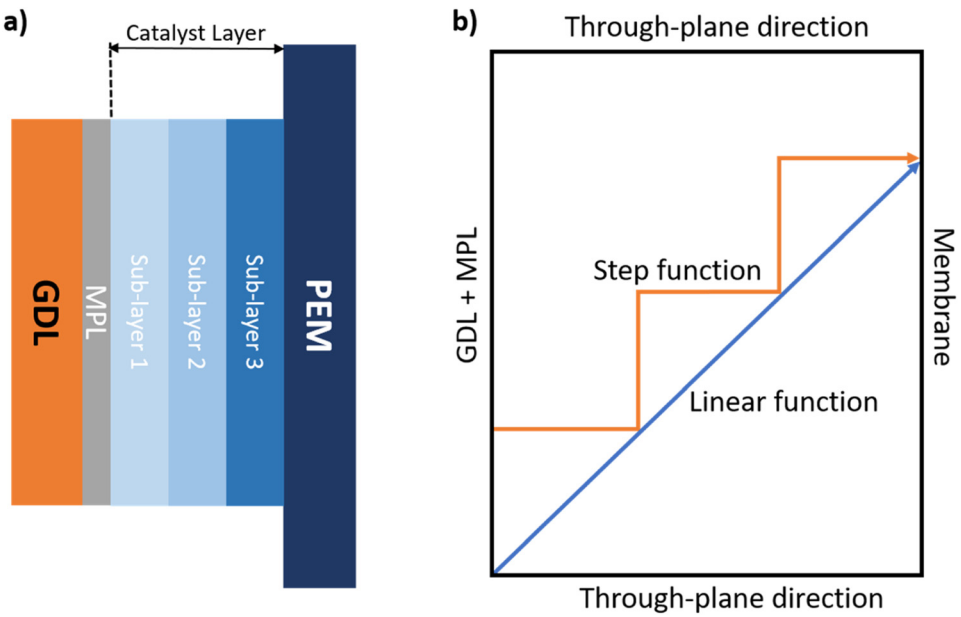

Fig. 2 a) Illustration of the cathode GDE with the CL divided into three theoretical sub-layers. b) Illustration of possible gradient functions: increasing step function and increasing linear function.

of the mask has been shown to influence the coating quality at the edges due to a shadowing effect.[47] Hence, a 1 mm-thick polycarbonate mask, with a coating area of 5 cm × 11 cm, was used during the deposition process (Fig. 1c).

Electrodes fabrication. As illustrated in Fig. 1a, nozzle 1 was exclusively used for spraying the Pt/C suspension, while nozzle 2 was dedicated to the Nafion dispersion. Each cathode GDE was structured into three theoretical sub-layers, as depicted in Fig. 2a, numbered sequentially from the MPL/CL interface to the CL/membrane interface. Within each sub-layer, the platinum content was maintained constant at 0.1 mg_{Pt} cm^{-2}, resulting in a total Pt loading of 0.3 mg_{Pt} cm^{-2} per GDE. The ionomer content, however, was varied between sub-layers by adjusting the number of spray passes from the Nafion nozzle. In this way, the I/C ratio of each sub-layer was finely tuned while keeping the Pt loading uniform throughout the catalyst layer.

It is worth noting that most of the experimental CL gradient designs reported in the literature are based on DCL smoothened step functions,[23,32,38,39] with only a few works reporting the use of three graded layers.[37] A major drawback of these methods is that they require preparing multiple inks with different formulations for each layer, which increases fabrication complexity and electrode-to-electrode variability. We adopted a manufacturing approach that utilizes separate, low-concentration dispersions for the catalyst and ionomer, along with a low flow rate to enhance control over the layer-by-layer deposition, allowing for the *in situ* formation of the TPB through a carefully tuned interfacial interaction. This method was specifically chosen to construct a TCL TP gradient design that closely approximates a linear gradient function (Fig. 2b). By precisely adjusting the deposition parameters and progressively varying the composition, the ionomer content can be smoothly modulated across the plane, enabling the formation of a more continuous and controlled through-plane gradient.

Three different GDEs were fabricated using this approach: GR1 featured a TP ionomer gradient increasing toward the membrane; GR2 had a reversed gradient, decreasing toward the membrane; and GR3 served as a control with a uniform I/C ratio throughout the entire catalyst layer. A summary of the I/C ratio variations across the sub-layers for each GDE is presented in Table 1.

The selected I/C values (0.4–1.2) span the range commonly reported for Pt/C cathode catalyst layers in PEMFCs and were chosen to represent low, intermediate, and high ionomer contents.[48–52] Both experimental[48–50] and modelling[50–52] studies have shown that this range reflects the balance between proton transport and oxygen diffusion within the catalyst layer, with low I/C ratios (0.4) favouring oxygen diffusion, intermediate values (0.8) commonly reported near optimal performance, and higher I/C ratios (1.2) improving proton transport at the expense of mass transport.

Table 1 I/C compositions for each sub-layer of three different samples: GR1, GR2 and GR3

	I/C sub-layer 1	I/C sub-layer 2	I/C sub-layer 3
GR1	0.4	0.8	1.2
GR2	1.2	0.8	0.4
GR3	0.8	0.8	0.8

Given that the concentrations of the two dispersions and their respective spraying flow rates were fixed, the ionomer content across the sub-layers was precisely modulated by varying the number of spray passes from the Nafion-dedicated nozzle relative to those from the Pt/C nozzle. This strategy enabled accurate control of the I/C ratio in each sub-layer while maintaining a consistent Pt loading throughout the catalyst layer. The process was validated using gravimetric mass measurements with a high-precision balance (Mettler Toledo, XPR106DUH/M). Following a few initial trials to determine the mass gain per spray cycle, we established the exact number of cycles required to achieve the target Pt loading for each sub-layer. Thanks to the automated syringe refill system integrated into the spray coater and managed *via* its software interface, the entire GDE fabrication process was fully automated. Each coating covered an area of 5 cm × 11 cm, resulting in two identical 25 cm^2 GDEs per batch, with an additional 5 cm × 1 cm section reserved for morphological and elemental characterization, including X-ray fluorescence (XRF) analysis. Fig. 2c provides a schematic representation of the TP ionomer gradient profiles applied to the three fabricated samples, each following a linear gradient function.

For comparison, a fourth GDE, named GD4, was fabricated with a uniform TP ionomer distribution using a conventional ink preparation method. The CL had an I/C ratio of 0.8 and a total Pt loading of 0.3 mg_{Pt} cm^{-2}. Specifically, 50 mg of Pt/C (20 wt% Pt) was dispersed in 200 mL of a 1 : 1 isopropanol : DI water mixture and sonicated for 20 min. Subsequently, 32 mg of Nafion was added to the dispersion, which was then left under continuous magnetic stirring overnight. Before deposition, the ink was placed in an ultrasonic bath for 30 min to ensure full homogenization. The ink was then spray-coated onto a 5 cm × 11 cm GDM substrate area under the exact same coating conditions used for the graded samples.

Fuel cell testing. A Gore Select membrane (GORE M765.08, USA), 8.5 μm thick, with an area of 36 cm^2 was used. Commercial GDEs (HyPlat, South Africa) with a Pt loading of 0.1 mg_{Pt} cm^{-2} were die cut to an area of 25 cm^2 and used as the anode electrodes. All in-house fabricated cathode GDEs were die-cut to a geometric area of 5 cm × 5 cm, identical to the HyPlat commercial anode GDEs. The MEA fabrication involved sandwiching a Gore Select membrane between a spray-coated cathode GDE with a platinum loading of 0.3 mg_{Pt} cm^{-2} and a commercial anode GDE with a platinum loading of 0.1 mg_{Pt} cm^{-2}. The MEA was hot-pressed between steel plates using a Carver hot press (USA) at 150 °C for 3 min under a pressure of 1250 psi. To prevent mechanical damage or misalignment during pressing, Kapton film sheets were placed between the MEA and the steel plates. Fuel cell testing was performed using a

cell with a 25 cm^2 active area (fuel cell fixtures from Scribner, USA). The setup consisted of stainless steel endplates, with PTFE sheets positioned between the endplates and gold-coated current collectors for electrical insulation. The graphite flow-field plates featured a triple-channel serpentine pattern, with both the channels and lands measuring approximately 1 mm in width and depth. PTFE gaskets were used on both sides of the MEA to ensure gas tightness and maintain appropriate compression, with bolts tightened to 4 N m torque. The pitch was maintained at around 25% of the total GDE thickness using Teflon gaskets with various thickness.

For performance evaluation, the assembled fuel cell was connected to a Scribner Associates 850e test station (Scribner, USA) equipped with a built-in potentiostat (Scribner 885) integrated with a frequency response analyser module for EIS measurements. All MEAs were conditioned identically by holding them at a constant voltage of 0.6 V for one hour, allowing the current to stabilize. The increasing current density was monitored during this period. Three polarization curves were recorded, and the MEA was considered fully conditioned or "broken-in" if the voltage deviation between consecutive curves was less than 5 mV, in line with U.S. DoE testing guidelines.[53] All MEA tests using in-house fabricated GDEs (GR1, GR2, GR3, GD4) were conducted at 80 °C. The anode and cathode were supplied with humidified hydrogen and air, respectively, at three different relative humidities (20%, 60%, and 100%) achieved by adjusting the dew points of both inlet gases (see Table S1). The tests were conducted in ascending RH order to minimize the risk of water accumulation within the cell. Reactant stoichiometries were set to 1.2 for hydrogen and 2.0 for air. Both anode and cathode outlets were maintained at atmospheric pressure with no applied backpressure. Electrochemical characterization included polarization curve measurements and cyclic voltammetry (CV) to evaluate electrochemically active surface area. Polarization data were collected from open-circuit voltage down to 0.3 V, in 0.025 V steps, with a 2 min hold at each voltage. The current from the final 30 s of each hold was averaged to represent the polarization response. For electrochemical surface area (ECSA) determination, nitrogen was flowed over the cathode at 0.2 L min^{-1} to purge residual oxygen until the OCV dropped below 0.15 V, at which point the flow was stopped. Hydrogen underpotential deposition charge was determined from the third CV cycle, measured between 0.06 V and 1.0 V at a scan rate of 20 mV s^{-1}. The ECSA was estimated using a conversion factor of 210 μC cm^{-2}. Before conducting the EIS measurements, the cells were operated at least for 10 min at 900 mA cm^{-2} to ensure stable operation in order to fulfil the stability and linearity requirements for accurate EIS analysis. The measurements were then carried out at 900 mA cm^{-2} over a frequency range of 10 kHz to 0.1 Hz, using 10 points per decade. EIS data at 20% RH are not reported, as the target current density could not be reached by all MEAs under this condition, preventing a valid and meaningful comparison with the 60% and 100% RH datasets.

The fuel cell durability test followed the ADT protocol recommended by the U.S. Department of Energy.[53] The procedure involved square-wave potential cycling between 0.6 V and 0.95 V, with a 3 s hold at each potential, for a total of 30 000 cycles. The test was conducted under H_2/N_2 conditions (anode/cathode) at fixed flow rates of 0.2 L min^{-1} each, at 80 °C, 100% relative humidity, and atmospheric pressure. Performance evaluations were carried out every 10 000 cycles using both CV and polarization curve measurements.

3. Results and discussion

Morphological and elemental analysis

The presence and distribution of gradients within the catalyst layers were examined using SEM-EDS spectrum imaging. Following overnight drying at 60 °C in a vacuum oven, a 1 cm × 1 cm section from each graded GDE samples was embedded in epoxy resin for cross-sectional analysis. EpoThin resin and hardener (Buehler) were used for embedding. Samples were placed within embedding molds and cured overnight under vacuum at room temperature. Once hardened, the cross-sections were sequentially ground using SiC abrasive papers (Struers GmbH) ranging from 500 to 4000 grain size. Subsequent polishing was carried out with an MD-Mol polishing plate and DiaPro Mol B diamond suspension, gradually decreasing particle size from 6 μm to 1 μm. To enhance conductivity, the prepared samples were gold-sputtered (Cressington 108 manual) and mounted using conductive copper tape (Plano GmbH). SEM images were obtained on a JEOL-6701F with an accelerating voltage of 10 kV and working distance of 8.0 mm, equipped with an Oxford Instruments EDS detector.

The presence of compositional gradients was assessed using SEM-EDX spectrum imaging, which provides the necessary spatial resolution and elemental contrast to detect TP variations in catalyst layers. Fig. 3 presents the fluorine and platinum signal profiles obtained from spectrum imaging for electrodes GR1 (a) and GR2 (b), which exhibit graded structures, and GR3 (c), characterized by a uniform composition. The first column displays SEM images of each sample, followed by EDS intensity profiles across the catalyst layer width, corresponding to the fluorine signal from the ionomer (red) and the platinum signal from the catalyst particles (dark grey). As shown in Fig. 3c, the GR3 sample, which features a constant I/C ratio of 0.8 throughout the CL, exhibits uniform fluorine and platinum signals, indicating a predominantly homogeneous distribution of ionomer and catalyst. In contrast, the intentionally graded samples shown in Fig. 3a and b exhibit a distinct and more pronounced TP gradient within the catalyst layer. For sample GR1, a continuous and linear increase in ionomer content is observed from the MPL interface toward the membrane, clearly indicating a controlled gradient. This behaviour confirms the effectiveness of the automated layer-by-layer approach, which employs small incremental coating steps

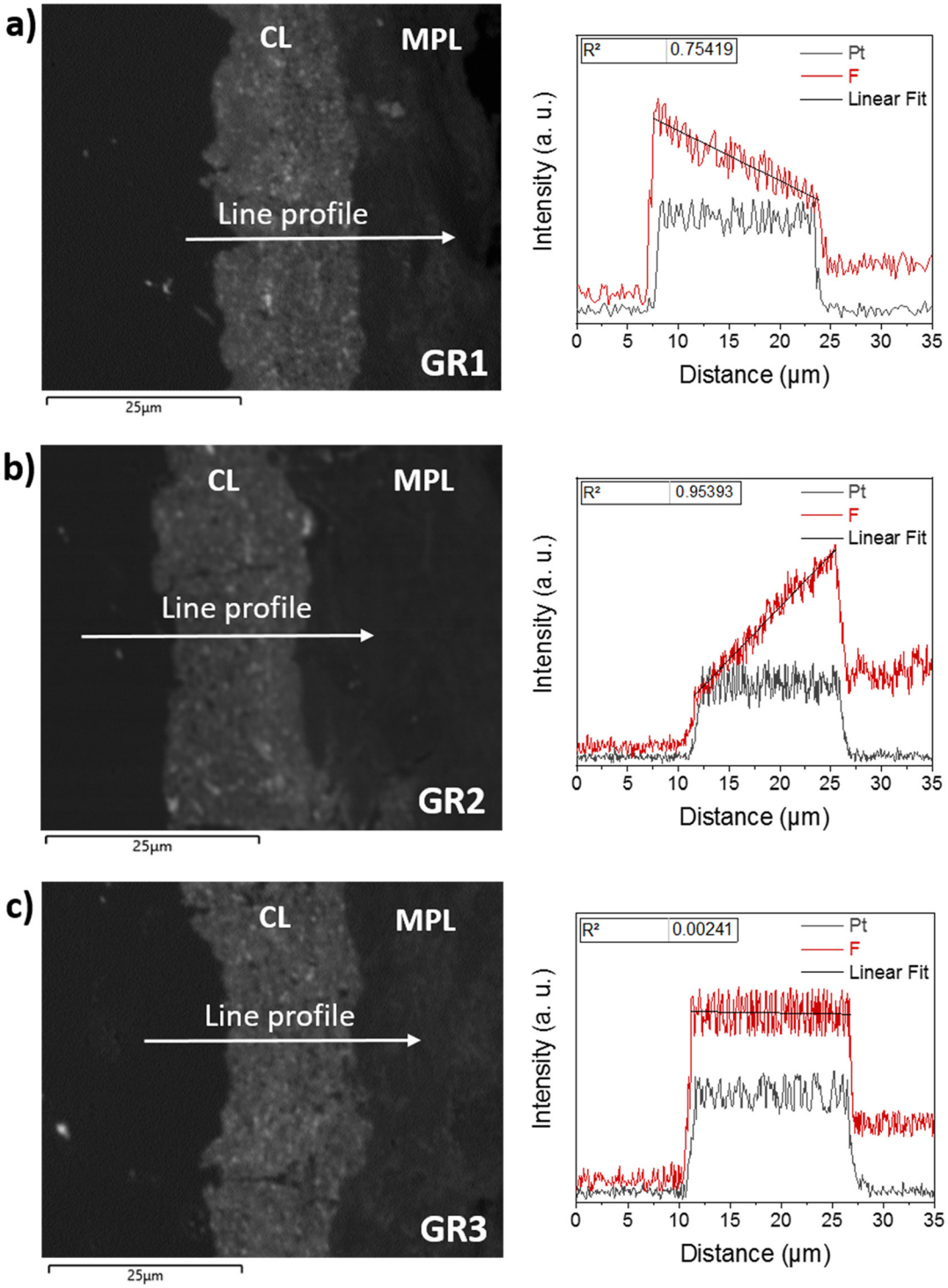

Fig. 3 SEM-EDS analysis of the three samples, including linear fits of the fluorine signal across the CL, a) GR1 b) GR2 c) GR3.

using diluted inks and low flow rates to construct a tailored TP composition. The linearity of the gradient strongly suggests that it is a direct result of the intentional manufacturing strategy, rather than an unintended consequence of natural gradients arising from the ink's water-to-alcohol ratio or the drying process.[54] A similar trend is observed for sample GR2 (Fig. 3b), which features an inverse gradient design. In this case, the ionomer content increases from the PEM toward the MPL interface. Here as well, the TP ionomer distribution approximates a linear function, further supporting the controlled nature of the fabrication method.

The EDS line scans were acquired with a spatial resolution of approximately 0.07–0.13 µm per point, corresponding to

several hundred data points across the catalyst layer thickness, ensuring a high-resolution compositional profile. To quantitatively assess the gradient linearity, a linear regression analysis of the fluorine signal (representative of the ionomer distribution) was performed as a function of distance. The resulting coefficients of determination (R^2) were 0.75 for GR1 and 0.95 for GR2, confirming a strong linear relationship between fluorine signal and position across the catalyst layer thickness. In contrast, the uniform sample GR3 exhibited $R^2 \approx 0$, consistent with the absence of a compositional gradient. These results quantitatively demonstrate that the ionomer distribution follows a smooth, continuous transition rather than discrete layered steps.

Moreover, *ex situ* XRF measurements were performed to determine the Pt loading of the electrodes (Malvern Panalytical, Epsilon 4). X-ray energy of 50 keV, measurement time of 30 s, and a focus distance of 1 mm were used. Calibration was performed using a three-point method with high-precision calibration standards (Micromatter Technologies). The quantified Pt loadings were 0.30 ± 0.01, 0.29 ± 0.01, and 0.31 ± 0.02 mg_{Pt} cm^{-2} for GR1, GR2, and GR3, respectively. The reported standard deviations were derived from nine spectra acquired at different locations across the GDE active area, ensuring a representative evaluation of the overall Pt distribution (see Fig. S1).

These measurements are fully consistent with the gravimetric estimates obtained using a high-precision balance, thereby confirming the reliability and accuracy of the fabrication process. Similarly, for GD4, with a measured loading of 0.31 ± 0.01 mg_{Pt} cm^{-2} the gravimetric estimation method proved to be accurate.

To further assess batch-to-batch reproducibility, XRF measurements were performed on three independently fabricated batches of GDEs. The Pt loadings were found to be highly consistent across batches, with variations within ±0.02 mg_{Pt} cm^{-2}, confirming the robustness of the deposition process. A summary of these results is provided in Table S2. XRF was selected for this analysis because it enables rapid, non-destructive quantification of Pt loading without requiring sample preparation, allowing efficient screening of multiple electrodes and measurement locations across different batches.

In addition lower magnification SEM images of samples GR1, GR2 and GR3 are presented in Fig. S2.

Electrochemical characterization

Following the confirmation of the TP ionomer gradient *via* EDS analysis, a performance comparison between CLs with gradient and uniform ionomer distributions is presented in Fig. 4. Tests were conducted under three different RH conditions: 100%, 60%, and 20%. The polarization curves (Fig. 4a–c) demonstrate that the gradient design in sample GR1 – featuring a higher ionomer content near the PEM – consistently delivers the best performance across all RH levels. At 100% RH, GR1 achieved peak power densities approximately 17% and 23% higher than those of the uniform and inverted gradient configurations, respectively. This performance advantage became even more pronounced under lower humidity conditions, with peak power increases of 29% to 42% at 20% RH compared to the other CL architectures. A similar trend was observed

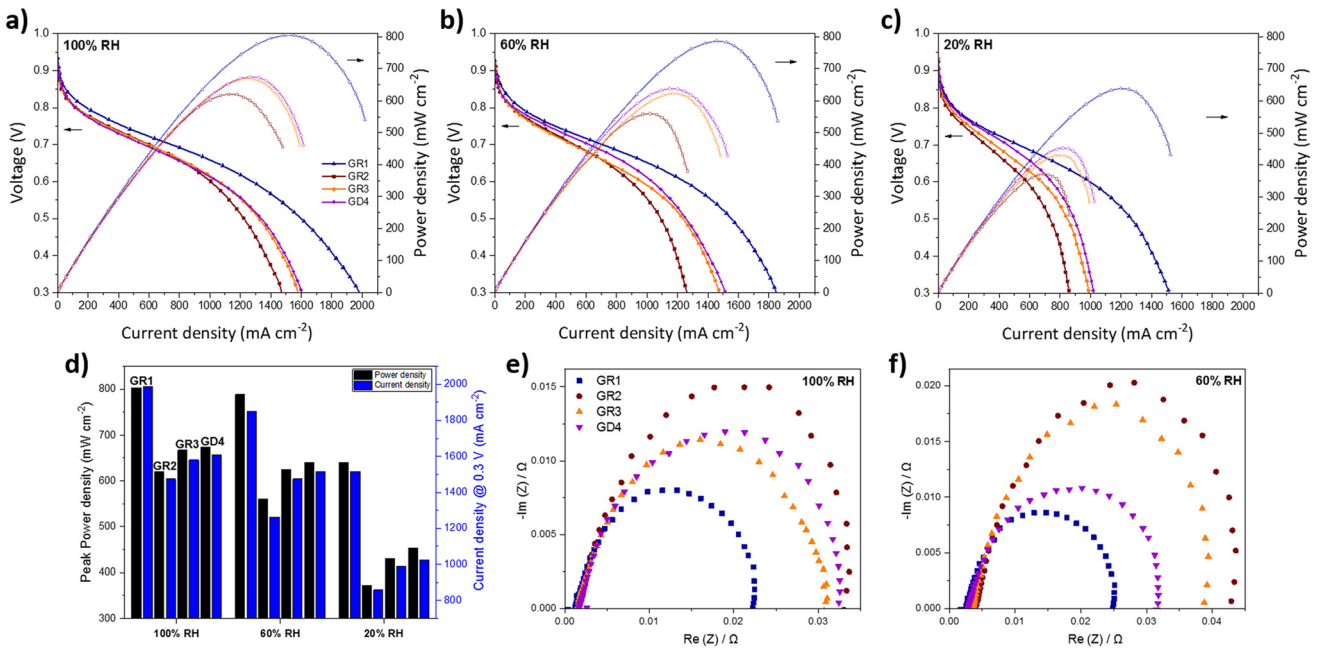

Fig. 4 Performance characterizations for 25 cm^2 single PEMFC, H_2/air 1.2/2, 80 °C, zero back-pressure, for samples GR1, GR2, GR3 and GD4. Polarisation curves at different RH: a) 100% b) 60% c) 20%; d) comparison of peak power density and current density at 0.3 V; EIS at 900 mA cm^{-2} e) at 100% RH and f) 60% RH.

in the maximum current densities across all humidity conditions. As shown in Fig. 4d, GR1 reached a maximum current density of approximately 2.0 A cm^{-2} at 0.3 V under 100% RH, compared to ~1.6 A cm^{-2} and ~1.5 A cm^{-2} for the uniform and inverted gradient designs, respectively. The performance gap further widened at reduced humidity levels, mirroring the trend seen in the power density data. This enhanced performance under varying RH levels for GR1 aligns with findings from Ayoub *et al.*,[55] who reported improved results for gradient CLs in a dual-layer TP design tested under different relative humidities. However, their approach required spraying multiple sub-layers with distinct ink formulations, a labor-intensive and less reproducible process that poses clear limitations for scalability and industrial adoption. In contrast, our method achieves an ionomer gradient without the added complexity of preparing several inks, offering a more robust, automatable, and scalable route that may ultimately deliver greater performance benefits.

It is worth noting that the catalyst layers with a uniform ionomer distribution and same I/C ratio, samples GR3 and GD4, exhibited comparable performance across the entire range of relative humidity conditions. This consistency further validates the effectiveness of the novel double-nozzle manufacturing approach, involving separated solutions for ionomer and catalyst.

The superior performance of GR1 can be attributed to its optimized ionomer distribution. The higher ionomer content near the PEM enhances proton conductivity, while the lower I/C ratio near the MPL facilitates gas transport to the TPB. The higher ionomer content toward the membrane not only facilitates H^+ transport within the CL, but also promotes reactant transport due to the resulting interparticle pore gradient in the opposite direction. This dual-direction gradient effect – improving both proton and reactant transport – results in significantly improved current densities, particularly at lower humidities (see Fig. 4d). Furthermore, the increased ionomer content near the PEM enhances water retention, resulting in higher water content at the membrane–CL interface. This configuration proves particularly beneficial, mitigating dehydration under low relative humidity conditions, and further amplifies the performance gap compared to the uniform and inverted gradient configurations. Conversely, the presence of an interparticle pore size gradient increasing toward the CL/MPL interface facilitates efficient removal of excess water, which improves the electrode's overall water management capabilities. In contrast, sample GR2, with a reverse ionomer gradient (*i.e.*, higher ionomer content near the MPL), exhibited the poorest performance across all RH conditions. This is likely due to increased mass transport resistance and reduced proton conductivity through the CL thickness. The EIS results at 0.9 A cm^{-2} (Fig. 4e and f) further highlight the superior performance of GR1, which exhibits the smallest high-frequency intercept and the most reduced semicircle diameter. These features correspond to a slightly lower ohmic resistance and a clearly reduced charge-transfer resistance compared to GR2, GR3, and GD4. Overall, the impedance analysis confirms the enhanced electrochemical behaviour of sample GR1 under both humidity conditions.

It is worth adding that these performance results, which align with the state of the art,[16,32,37–39,55] serve as intrinsic evidence that the manufacturing approach is effective. By depositing the catalyst and ionomer separately, this method enables the *in situ* formation of the TPB and supports the development of a more controlled and interconnected catalyst layer microstructure. A similar approach has been reported in the literature, where a non-covered catalyst/ionomer interfacial structure was designed to minimize proton resistance and enhance oxygen transport by avoiding dense ionomer coverage on Pt surfaces.[56] In addition, the fact that GR3 – fabricated using this layer-by-layer approach – exhibits performance comparable to its counterpart, GD4, produced *via* a conventional ink-based method (under identical I/C ratio and coating conditions), further validates the effectiveness of this fabrication method.

Moreover, all the performance results presented are fully consistent with the ECSA trends observed for the four samples under different relative humidity conditions. Fig. 5a–c show the CV profiles of GR1, GR2, GR3, and GD4 at 100%, 60%, and 20% RH, respectively. GR1 consistently exhibits the highest ECSA across all RH levels, while GR2 shows the lowest, in alignment with the power and current densities performance data, despite all samples having the same Pt loading. Additionally, it is evident that the ECSA values for all four samples generally increase with rising relative humidity. This trend has also been reported by Fan *et al.*,[57] who primarily attributed the increase in ECSA to enhanced contact between Pt particles and water domains, rather than the formation of new proton transport pathways.

To further assess the performance of these novel engineered catalyst layers, an ADT was conducted to evaluate the long-term durability of the gradient (GR1 and GR2) and uniform (GR3 and GD4) TP ionomer distribution CLs. As previously discussed, conventional gradient designs often suffer from interfacial defects due to abrupt material transitions. In contrast, the gradual and nearly linear TP gradient achieved in this work avoids such sharp interfaces, thereby enhancing mechanical integrity and potentially improving durability.

In discrete step-gradient architectures (*e.g.* DCL or TCL), abrupt compositional interfaces can introduce localized variations in ionomer content, porosity, and transport properties, leading to non-uniform current distribution and water management during operation. From a transport perspective, such discontinuities can introduce additional interfacial resistances by disrupting the continuity of proton-conducting pathways and hindering oxygen transport across the interface, resulting in locally increased overpotentials and heterogeneous reaction environments.[9,58] In contrast, the continuous gradient structure produced here, supported by the linear EDS profiles and corresponding regression analysis

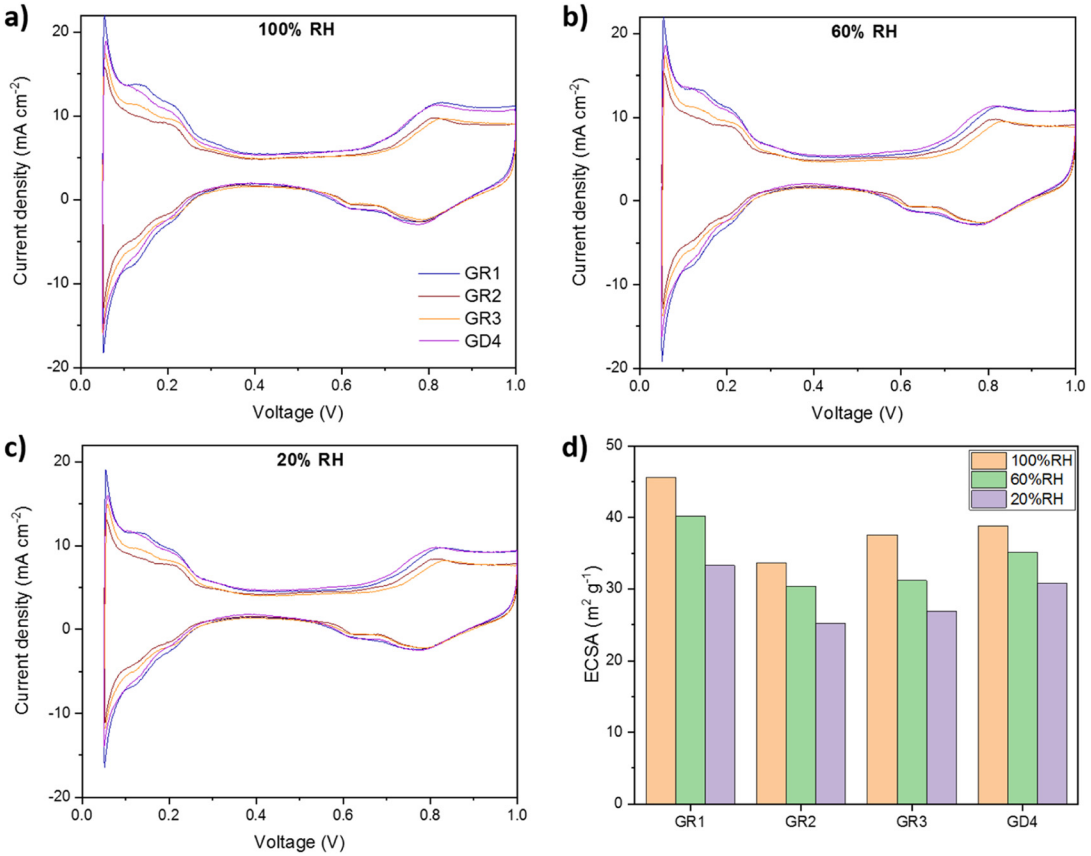

Fig. 5 ECSA characterizations 25 cm^2 single PEMFC, H_2/N_2 0.2 L min^{-1}, 80 °C, no back-pressure for samples GR1, GR2, GR3 and GD4. CVs profiles acquired, between 0.05–1 V with 20 mV s^{-1} scan rate, at different RH: a) 100%, b) 60%, and c) 20%; d) comparison of ECSA values at different RH.

(Fig. 3), provides a smooth transition in composition across the catalyst layer thickness, promoting more homogeneous reaction conditions and mitigating localized degradation phenomena. Fig. 6 presents the polarization curves obtained during the ADT, following the U.S. DoE testing protocol,[53] for all four samples.

At the beginning of testing, GR1, the gradient-engineered sample with increasing ionomer content toward the PEM, demonstrated a peak power density of 803 mW cm^{-2} and a limiting current density of 1990 mA cm^{-2} (Fig. 6a). This performance exceeded that of both the uniform ionomer configuration (Fig. 6c and d) and the inverted gradient design (Fig. 6b), which achieved peak power densities of 620 mW cm^{-2} and limiting current densities of 1480 mA cm^{-2} under the same conditions (80 °C, no backpressure, H_2/air stoichiometry 1.2/2). During the first 10 000 ADT cycles, the MEAs with uniform ionomer distribution (GR3 and GD4) showed moderate degradation, 12% and 11% reductions in peak power, respectively. In contrast, GR2, featuring an ionomer increasing gradient directed toward the MPL, experienced a significantly larger 23% drop in performance. GR1, despite undergoing the same aggressive chemical and mechanical stresses, exhibited the highest durability, retaining 94% of its initial performance after 10 000 cycles and showing only a 23% decrease after 30 000 cycles. This was notably better than GR3 and GD4, which degraded by 29% and 26%, respectively, over the full ADT period. GR2 showed the poorest durability, with a 35% decline, resulting in a final limiting current density below 1000 mA cm^{-2} and a peak power output of just 402 mW cm^{-2}.

These findings suggest that the smooth, gradual ionomer gradient in GR1 not only improves performance at low relative humidity, due to enhanced proton transport and water management, but also significantly enhances long-term durability. The more optimal material distribution within the CL promotes a favourable local environment at the CL/PEM interface by increasing water availability where proton conduction is most critical, while simultaneously improving gas transport at the CL/MPL interface through increased interparticle porosity. This dual-gradient structure effectively mitigates microstructural degradation, which would otherwise lead to rapid performance loss. This is further supported by the ECSA analysis, which shows improved ECSA retention for GR1, indicating reduced catalyst degradation. The more uniform reaction environment enabled by the continuous gradient is expected to limit localized current density hotspots, thereby suppressing Pt dissolution–redeposition, particle agglomeration, and carbon support corrosion. In addition, the absence of abrupt compositional interfaces may reduce mechanical stresses

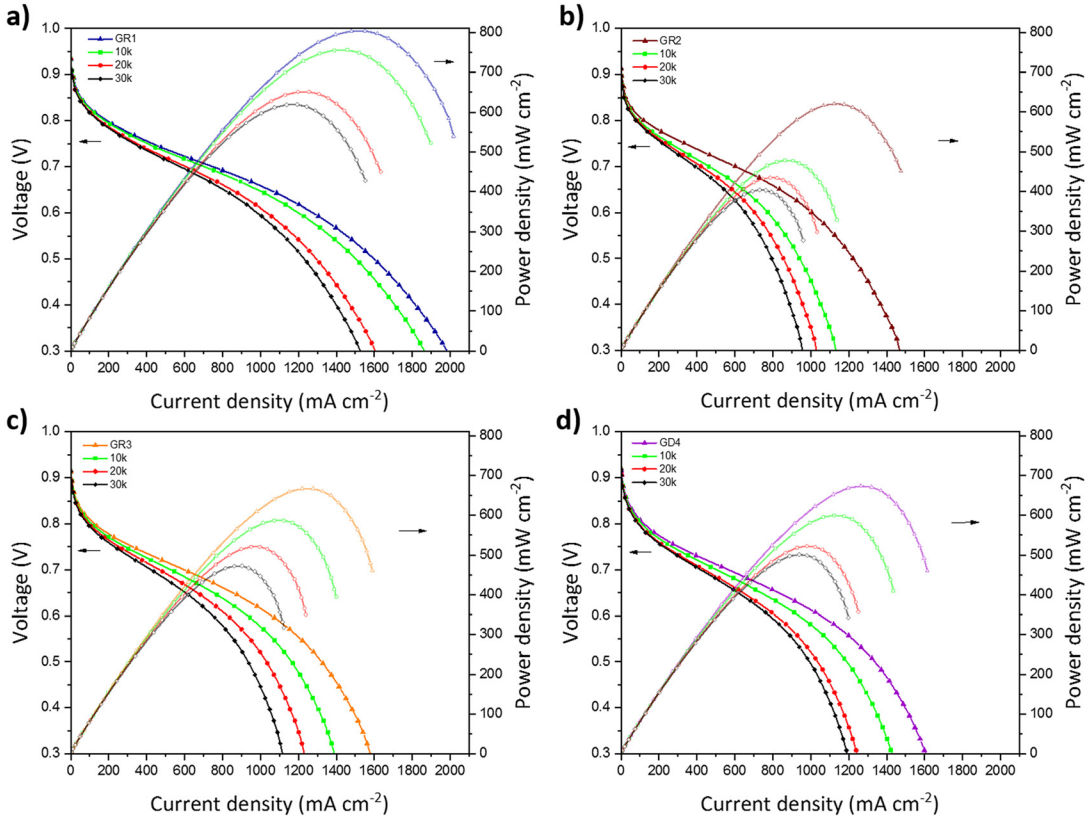

Fig. 6 Polarisation curves for 25 cm^2 single PEMFC, H_2/air 1.2/2, 80 °C, zero back-pressure, during the ADT protocol, 30k potential cycles between 0.6 V and 0.95 V, in H_2/N_2, 0.2 L min^{-1}, 80 °C, 100% RH, for samples: a) GR1, b) GR2, c) GR3 and d) GD4.

associated with ionomer swelling and shrinkage during potential cycling, further contributing to the enhanced structural stability of the catalyst layer.

Therefore, carefully balancing material distribution within the CL is essential to achieving optimal proton conduction near the PEM, further supported by the ionomer's water retention capacity, and minimizing mass transport resistance near the MPL. The controlled construction of this dual-gradient structure within the CL is a key factor in advancing both performance and operational lifetime of PEM fuel cells.

Furthermore, Fig. 7 illustrates the ECSA loss during the ADT, calculated from the CV profiles of the four samples at BOL, 10k, 20k, and 30k cycles (see Fig. S3). As expected, the ECSA degradation trends closely mirror those observed in the polarization curve analysis. GR1 exhibited the highest initial ECSA value (45.6 m^2 g^{-1}) and maintained a strong retention of 69% after 30 000 cycles. In contrast, GR2 showed

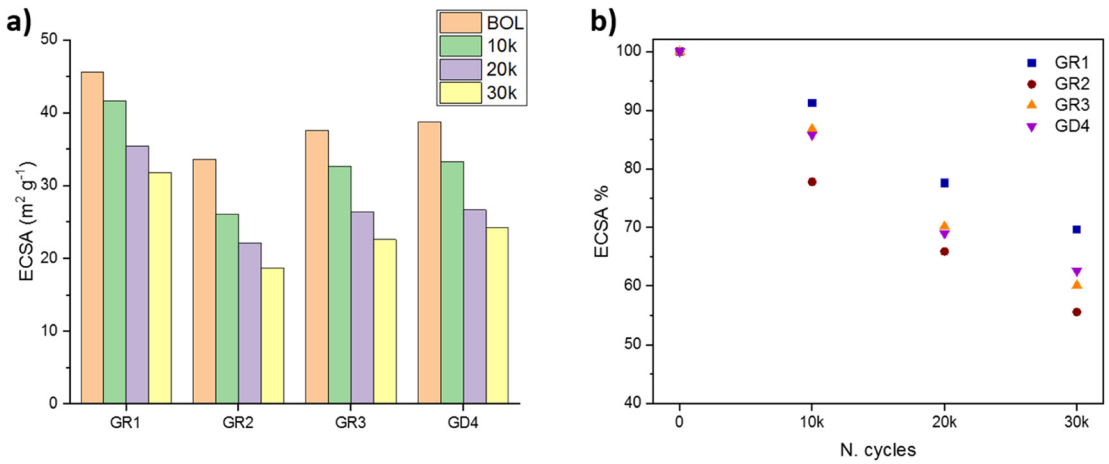

Fig. 7 ECSA loss for samples GR1, GR2, GR3 and GD4 during the ADT; a) absolute ECSA b) ECSA%.

significant degradation early in the test, with a ~23% ECSA loss after just 10k cycles and a total loss of 45% by the end of the ADT, decreasing from 33.6 $m^2 g^{-1}$ to 18.7 $m^2 g^{-1}$, closely reflecting its performance decline in polarization measurements. For the catalyst layers with uniform ionomer distribution (GR3 and GD4), initial ECSA values were comparable at 37.6 $m^2 g^{-1}$ and 38.8 $m^2 g^{-1}$, respectively. After 30k cycles, GR3 retained 60% of its ECSA, while GD4 retained 62%. Notably, GR1 demonstrated the lowest total ECSA loss (~31%) over the entire ADT, which is fully consistent with its superior power density retention, reinforcing the advantages of the engineered gradient structure.

4. Conclusions

This work presents an innovative approach to fabricating continuously graded CLs using a dual-nozzle spray-coating technique capable of precisely controlling the ionomer-to-carbon ratio through the catalyst layer thickness. The resulting TP gradient enables a non-uniform ionomer distribution that simultaneously improves proton conductivity, oxygen diffusion, mass transport, and water management. Beyond the linear gradient demonstrated here, this method lays the groundwork for developing more complex, tailored microstructural architectures through in-process material tuning.

In summary, a graded catalyst–ionomer interface offers a promising pathway to optimize the structural and functional transition from the PEM through the CL to the MPL. By introducing a smooth and continuous ionomer gradient, proton transport is effectively directed toward regions of high oxygen reduction reaction activity near the membrane, while water removal and oxygen access are facilitated in zones with lower catalytic demand, such as at the CL/MPL interface. Importantly, the increased ionomer concentration near the PEM also enhances water retention precisely where it is most critical, mitigating dehydration-related degradation and significantly boosting performance, particularly under low relative humidity conditions.

Experimental results confirm the clear advantages of this gradient design. The optimal configuration of sample GR1 (with a higher ionomer-to-carbon (I/C) ratio near the membrane) achieved a peak power density of 803 mW cm^{-2} and a limiting current density of 1990 mA cm^{-2} at 80 °C and ambient pressure, outperforming the baseline uniform CL (sample GR3, I/C = 0.8), which reached only 667 mW cm^{-2} and 1591 mA cm^{-2}, respectively. Under ADT, the gradient-optimized CL showed markedly improved durability, with only a 23% loss in peak power and a 31% reduction in ECSA after 30 000 cycles, substantially better than the uniform and inverted designs.

These findings suggest that the CL and PEM should not be treated as isolated functional layers, but rather as a continuous, interdependent system. This integrated view envisions a compound architecture with low pore space and high ionomer content at the PEM interface for optimal ionic contact, gradually transitioning to a highly porous, low-ionomer region toward the CL/MPL for improved gas transport and water management.

The continuous gradient catalyst layer strategy offers a scalable, high-performance alternative to conventional designs, opening new avenues for next-generation proton exchange membrane fuel cells with significantly enhanced efficiency, durability, and water management capabilities.

Conflicts of interest

There are no conflicts to declare.

Data availability

Data for this article, including electrochemical data, are available at the UCL Data Repository at https://doi.org/10.5522/04/31288483.

Supplementary information (SI) is available. See DOI: https://doi.org/10.1039/d6lf00036c.

Acknowledgements

This work was supported by funding from the UK Engineering and Physical Sciences Research Council (EPSRC) – EP/W03395X/1, EP/X023656/1, EP/W033321/1.

References

1 T. A. Suter, K. Smith, J. Hack, L. Rasha, Z. Rana and G. M. A. Angel, *et al.*, Engineering catalyst layers for next-generation polymer electrolyte fuel cells: a review of design, materials, and methods, *Adv. Energy Mater.*, 2021, **11**, 2101025.
2 K. Smith, F. Foglia, A. J. Clancy, D. J. Brett and T. S. Miller, Nafion matrix and ionic domain tuning for high-performance composite proton exchange membranes, *Adv. Funct. Mater.*, 2023, **33**, 2304061.
3 Y. Li, Z. Wu, C. Wang, X. Yu, W. Gao and B. Wang, *et al.*, Engineering triple-phase boundary in Pt catalyst layers for proton exchange membrane fuel cells, *Adv. Funct. Mater.*, 2024, **34**, 2310428.
4 Y. Sun, S. Polani and F. Luo, *et al.*, Advancements in cathode catalyst and cathode layer design for proton exchange membrane fuel cells, *Nat. Commun.*, 2021, **12**, 5984.
5 F. Zhang, B. Zu, B. Wang, Z. Qin, J. Yao and Z. Wang, *et al.*, Developing long-durability proton-exchange membrane fuel cells, *Joule*, 2025, **9**, 101853.
6 S. Jang, Y. S. Kang, D. Kim, S. Park, C. Seol and S. Lee, *et al.*, Multiscale architectured membranes, electrodes, and transport layers for next-generation polymer electrolyte membrane fuel cells, *Adv. Mater.*, 2023, **35**, 2204902.
7 S. Zhou, M. P. Tudball, Y. Guo, B. Brandt, A. Zucconi and W. Du, *et al.*, Coordinated multi-component gradient engineering of catalyst layers for advanced polymer electrolyte fuel cells, *Adv. Funct. Mater.*, 2025, e18360.
8 K. Khedekar, M. Rezaei Talarposhti, M. M. Besli, S. Kuppan, A. Perego and Y. Chen, *et al.*, Probing heterogeneous degradation of catalyst in PEM fuel cells under realistic automotive conditions with multi-modal techniques, *Adv. Energy Mater.*, 2021, **11**, 2101794.

9 L. Xing, W. Shi, H. Su, Q. Xu, P. K. Das, B. Mao and K. Scott, Membrane electrode assemblies for PEM fuel cells: a review of functional graded design and optimization, *Energy*, 2019, **177**, 445–464.
10 M. Ayoub, T. Böhm, M. Bierling, S. Thiele and M. Brodt, Review—Graded catalyst layers in hydrogen fuel cells: a pathway to application-tailored cells, *J. Electrochem. Soc.*, 2024, **171**, 094503.
11 Q. Liu, B. Wang, Z. Ling, Y. Zhou, S. Hu, X. Fu, R. Zhang, Y. Zhang, F. Zhao, X. Li, N. Li and J. Yang, Natural clay frameworks in membrane electrode assembly: Challenges and perspectives, *Nano Energy*, 2025, **139**, 110980.
12 B. Wang, Z. Ling, Q. Liu, X. Fu, R. Zhang, S. Hu, F. Zhao, X. Li, X. Bao, N. Li and J. Yang, Phosphoric Acid-in-Clay Electrolyte Boosting Polybenzimidazole Membranes for High-Performance Fuel Cells, *Adv. Funct. Mater.*, 2026, **36**, e18482.
13 G. Varghese, T. V. Joseph and P. Chippar, Optimization of graded catalyst layer to enhance uniformity of current density and performance of high temperature-polymer electrolyte membrane fuel cell, *Int. J. Hydrogen Energy*, 2022, **47**, 4018–4032.
14 M. Santis, S. A. Freunberger, A. Reiner and F. Büchi, Homogenization of the current density in polymer electrolyte fuel cells by in-plane cathode catalyst gradients, *Electrochim. Acta*, 2006, **51**, 5383–5393.
15 D. P. Wilkinson and J. St-Pierre, In-plane gradients in fuel cell structure and conditions for higher performance, *J. Power Sources*, 2003, **113**, 101–108.
16 L. Yang, K. Fu, X. Jin, S. Wang, Q. Gan and Q. Zhang, *et al.*, Catalyst layer design with inhomogeneous distribution of platinum and ionomer optimal for proton exchange membrane fuel cell cold-start, *Chem. Eng. Sci.*, 2022, **263**, 118132.
17 M. Prasanna, E. A. Cho, H. J. Kim, I. H. Oh, T. H. Lim and S. A. Hong, Performance of proton-exchange membrane fuel cells using the catalyst-gradient electrode technique, *J. Power Sources*, 2007, **166**, 53–58.
18 Y. Zhang, A. Smirnova, A. Verma and R. Pitchumani, Design of a proton exchange membrane (PEM) fuel cell with variable catalyst loading, *J. Power Sources*, 2015, **291**, 46–57.
19 H. Arai, E. Yoshida, H. Ito and N. Katayama, Segmentation of PEM fuel cell catalyst layer via electrospray deposition, *Chem. Eng. Sci.*, 2025, **316**, 121898.
20 S. Herden, F. Riewald, J. A. Hirschfeld and M. Perchthaler, In-plane structuring of proton exchange membrane fuel cell cathodes: effect of ionomer equivalent weight structuring on performance and current density distribution, *J. Power Sources*, 2017, **355**, 36–43.
21 Y. Liu, C. Ji, W. Gu, D. R. Baker, J. Jorne and H. A. Gasteiger, Proton conduction in PEM fuel cell cathodes: effects of electrode thickness and ionomer equivalent weight, *J. Electrochem. Soc.*, 2010, **157**, B1154–B1161.
22 F. C. Cetinbas, S. G. Advani and A. K. Prasad, Investigation of a polymer electrolyte membrane fuel cell catalyst layer with bidirectionally graded composition, *J. Power Sources*, 2014, **270**, 594–602.
23 G. Y. Chen, C. Wang, Y. J. Lei, J. Zhang, Z. Mao and Z. Q. Mao, *et al.*, Gradient design of Pt/C ratio and Nafion content in cathode catalyst layer of PEMFCs, *Int. J. Hydrogen Energy*, 2017, **42**, 29960–29965.
24 D. Song, Q. Wang, Z. Liu, M. Eikerling, Z. Xie, T. Navessin and S. Holdcroft, A method for optimizing distributions of Nafion and Pt in cathode catalyst layers of PEM fuel cells, *Electrochim. Acta*, 2005, **50**, 3347–3358.
25 P. Jain, L. T. Biegler and M. S. Jhon, Optimization of polymer electrolyte fuel cell cathodes, *Electrochem. Solid-State Lett.*, 2008, **11**, B193–B195.
26 R. Fan, G. Chang, Y. Xu and J. Xu, Investigating and quantifying the effects of catalyst layer gradients, operating conditions, and their interactions on PEMFC performance through sensitivity analysis, *Energy*, 2024, **290**, 130128.
27 H. N. Su, Q. Zeng, S. J. Liao and Y. N. Wu, High performance membrane electrode assembly with ultra-low platinum loading prepared by a novel multi catalyst layer technique, *Int. J. Hydrogen Energy*, 2010, **35**, 10430–10436.
28 M. Srinivasarao, D. Bhattacharyya and R. Rengaswamy, Optimization studies of a polymer electrolyte membrane fuel cell with multiple catalyst layers, *J. Power Sources*, 2012, **206**, 197–203.
29 L. Xing, W. Shi, P. K. Das and K. Scott, Inhomogeneous distribution of platinum and ionomer in the porous cathode to maximize the performance of a PEM fuel cell, *AIChE J.*, 2017, **63**, 4895–4910.
30 M. Srinivasarao, D. Bhattacharyya, R. Rengaswamy and S. Narasimhan, Performance analysis of a PEM fuel cell cathode with multiple catalyst layers, *Int. J. Hydrogen Energy*, 2010, **35**, 6356–6365.
31 M. Secanell, R. Songprakorp, N. Djilali and A. Suleman, Optimization of a proton exchange membrane fuel cell membrane electrode assembly, *Struct. Multidiscip. Optim.*, 2010, **40**, 563–583.
32 H. Nguyen, D. Sultanova, P. A. Heizmann, S. Vierrath and M. Breitwieser, Improving the efficiency of fully hydrocarbon-based proton-exchange membrane fuel cells by ionomer content gradients in cathode catalyst layers, *Mater. Adv.*, 2022, **3**, 8460–8468.
33 S. M. Jayawickrama, D. Wu, R. Nakayama, S. Ishikawa, X. Liu and G. Inoue, *et al.*, Effect of a polybenzimidazole coating on carbon supports for ionomer content optimization in polymer electrolyte membrane fuel cells, *J. Power Sources*, 2021, **496**, 229855.
34 H. Ishikawa, Y. Sugawara, G. Inoue and M. Kawase, Effects of Pt and ionomer ratios on the structure of catalyst layer: a theoretical model for polymer electrolyte fuel cells, *J. Power Sources*, 2018, **374**, 196–204.
35 D. Gerteisen, Impact of inhomogeneous catalyst layer properties on impedance spectra of polymer electrolyte membrane fuel cells, *J. Electrochem. Soc.*, 2015, **162**, F1431–F1437.
36 Q. Wang, M. Eikerling, D. Song, Z. Liu, T. Navessin, Z. Xie and S. Holdcroft, Functionally graded cathode catalyst layers

for polymer electrolyte fuel cells: I. Theoretical modeling, *J. Electrochem. Soc.*, 2004, **151**, A950–A957.

37 Z. Xie, T. Navessin, K. Shi, R. Chow, Q. Wang and D. Song, *et al.*, Functionally graded cathode catalyst layers for polymer electrolyte fuel cells: II. Experimental study of the effect of Nafion distribution, *J. Electrochem. Soc.*, 2005, **152**, A1171–A1179.

38 K.-H. Kim, H. J. Kim, K. J. Lee, J. H. Jang, S. Y. Lee, E. Cho, I. H. Oh and T. H. Lim, Effect of Nafion® gradient in dual catalyst layer on proton exchange membrane fuel cell performance, *Int. J. Hydrogen Energy*, 2008, **33**, 2783–2789.

39 S. Shahgaldi, A. Ozden, X. Li and F. Hamdullahpur, Cathode catalyst layer design with gradients of ionomer distribution for proton exchange membrane fuel cells, *Energy Convers. Manage.*, 2018, **171**, 1476–1486.

40 J. Shin, M. Son, S.-I. Kim, S. A. Song and D. H. Lee, Design of multi-layered gradient catalysts for efficient proton exchange membrane fuel cells, *J. Power Sources*, 2023, **582**, 233546.

41 H. Liu, L. Ney, N. Zamel and X. Li, Effect of catalyst ink and formation process on the multiscale structure of catalyst layers in PEM fuel cells, *Appl. Sci.*, 2022, **12**, 3776.

42 S. M. Andersen, Nano carbon supported platinum catalyst interaction behavior with perfluorosulfonic acid ionomer and their interface structures, *Appl. Catal. B: Environ.*, 2016, **181**, 146–155.

43 F. Zhou, H. Zhang, S. Guan, G. Li, L. Xia and M. Pan, Experimental probing of the effect of PFSA ionomer poisoning at different Pt loadings in a PEMFC, *J. Catal.*, 2022, **414**, 330–335.

44 M. Tang, H. Yan, X. Zhang, Z. Zheng and S. Chen, Materials strategies tackling interfacial issues in catalyst layers of proton exchange membrane fuel cells, *Adv. Mater.*, 2023, **35**, 2306387.

45 S.-H. Lee, S. H. Woo, B. J. Pak, S. Kim, Y. S. Kang and S. Woo, *et al.*, Ink droplet drying analysis for understanding the ink-catalyst layer transition in proton exchange membrane fuel cells, *J. Power Sources*, 2023, **585**, 233644.

46 J. Lee, H. Lee, J. H. Kim, T. A. Pham, S. Jang and S. M. Kim, Investigation of optimized spraying process for directly coated electrode in polymer electrolyte membrane fuel cell, *J. Ind. Eng. Chem.*, 2024, **132**, 474–481.

47 Z. Turtayeva, F. Xu, J. Dillet, K. Mozet, R. Peignier, A. Celzard and G. Maranzana, Manufacturing catalyst-coated membranes by ultrasonic spray deposition for PEMFC: identification of key parameters and their impact on performance, *Int. J. Hydrogen Energy*, 2022, **47**, 16165–16178.

48 Y. V. Yakovlev, Y. V. Lobko, M. Vorokhta, J. Nováková, M. Mazur, I. Matolínová and V. Matolín, Ionomer content effect on charge and gas transport in the cathode catalyst layer of proton-exchange membrane fuel cells, *J. Power Sources*, 2021, **490**, 229531.

49 A. Kobayashi, T. Fujii, C. Harada, E. Yasumoto, K. Takeda, K. Kakinuma and M. Uchida, Effect of Pt and Ionomer Distribution on Polymer Electrolyte Fuel Cell Performance and Durability, *ACS Appl. Energy Mater.*, 2021, **4**, 2307–2317.

50 L. Xian, Z. Wang, B. Chen, Z. Li, G. Liu, L. Chen and W. Q. Tao, Effect of ionomer content on fuel cell performance and mass transport under different Pt loadings: Experimental and molecular simulation study, *Renewable Energy*, 2026, **263**, 125522.

51 W. Wang, Z. Qu, X. Wang and J. Zhang, A Molecular Model of PEMFC Catalyst Layer: Simulation on Reactant Transport and Thermal Conduction, *Membranes*, 2021, **11**, 148.

52 W. Olbrich, T. Kadyk, U. Sauter, M. Eikerling and J. Gostick, Structure and conductivity of ionomer in PEM fuel cell catalyst layers: a model-based analysis, *Sci. Rep.*, 2023, **13**, 14127.

53 T. Abdel-Baset, T. Benjamin, R. Borup, K. E. Martin, N. Garland and S. Hirano, *et al.*, *Fuel Cell Technical Team Roadmap*, U.S. Department of Energy, 2017, Available at: https://www.energy.gov/sites/prod/files/2017/11/f46/FCTT_Roadmap_Nov_2017_FINAL.pdf.

54 T. V. Cleve, S. Khandavalli, A. Chowdhury, S. Medina, S. Pylypenko and M. Wang, *et al.*, Dictating Pt-based electrocatalyst performance in polymer electrolyte fuel cells, from formulation to application, *ACS Appl. Mater. Interfaces*, 2019, **11**, 46953–46964.

55 M. Ayoub, A. T. S. Freiberg, T. Böhm, A. Körner, A. Hutzler, S. Thiele and M. Brodt, Continuous graded catalyst layers for PEM fuel cells with improved humidity range tolerance, *J. Electrochem. Soc.*, 2024, **171**, 114503.

56 F. Chen, L. Guo, D. Long, S. Luo, Y. Song and M. Wang, *et al.*, Overcoming the limitation of ionomers on mass transport and Pt activity to achieve high-performing membrane electrode assembly, *J. Am. Chem. Soc.*, 2024, **146**, 30388–30396.

57 L. Fan, K. Wu, C. Tongsh, M. Zhu, X. Xie and K. Jiao, Mechanism of water content on the electrochemical surface area of the catalyst layer in the proton exchange membrane fuel cell, *J. Phys. Chem. Lett.*, 2019, **10**, 6409–6413.

58 S. Woo, S. Lee, A. Z. Taning, T.-H. Yang, S.-H. Park and S.-D. Yim, Current understanding of catalyst/ionomer interfacial structure and phenomena affecting the oxygen reduction reaction in cathode catalyst layers of proton exchange membrane fuel cells, *Curr. Opin. Electrochem.*, 2020, **21**, 289–296.